



Article

Modeling and Research on Railway Balise Transmission System for Underwater Debris

Ke Ye ^{1,*} , Jingpin Jiao ², Qing Xu ³, Fanghua Chen ¹  and Linfu Zhu ^{4,5}

¹ College of Mechanical & Energy Engineering, Beijing University of Technology, Beijing 100124, China; b202276060@emails.bjut.edu.cn

² School of Information Science and Technology, Beijing University of Technology, Beijing 100124, China; jiaojp@bjut.edu.cn

³ Beijing National Railway Research and Design Institute of Signal and Communication Group Co., Ltd., Beijing 100070, China; xuqing@crscd.com.cn

⁴ Standards & Metrology Research Institute, China Academy of Railway Sciences Corporation Limited, Beijing 100081, China; zhulinfu2008@163.com

⁵ China Railway Test & Certification Center, Beijing 100081, China

* Correspondence: yesky@emails.bjut.edu.cn

Abstract: The balise transmission system (BTS) is essential for train position sensing and safe operation. Transmission loss is a key parameter particularly required for the evaluation of systems. The eddy current loss (ECL), caused by the conductivity of debris, affects the transmission performance of the BTS when the balise is immersed in water. This study proposes an effective modeling for the BTS using S-parameters. Utilizing the electromagnetic coupling analysis in the near-field region, we derived an equivalent circuit with the frequency and conductivity of water taken into consideration. The S₂₁ can be predicted accurately by using the proposed equivalent circuit. For validation, a BTS system was implemented and measured to compare with theoretically calculated results and electromagnetic simulation results in the main lobe zone. The measurement results, simulation, and calculation were in good agreement. Moreover, the modeling was used to predict the I/O characteristics of the balise. The power of the balise uplink FSK signal was measured in the water debris and found to be approximately 0.62 dB less than in air. These findings aligned well with theoretical predictions.

Keywords: balise transmission system; electromagnetic coupling; S-parameters; water; equivalent circuit model



Citation: Ye, K.; Jiao, J.; Xu, Q.; Chen, F.; Zhu, L. Modeling and Research on Railway Balise Transmission System for Underwater Debris. *Appl. Sci.* **2024**, *14*, 7306. <https://doi.org/10.3390/app14167306>

Academic Editors: Valerio De Martinis and Raimond Matthias Wüst

Received: 20 July 2024

Revised: 12 August 2024

Accepted: 17 August 2024

Published: 19 August 2024



Copyright: © 2024 by the authors. Licensee MDPI, Basel, Switzerland. This article is an open access article distributed under the terms and conditions of the Creative Commons Attribution (CC BY) license (<https://creativecommons.org/licenses/by/4.0/>).

1. Introduction

As a dedicated near-field wireless communication system for railways, the BTS efficiently facilitates secure information transmission between the ground balise and onboard equipment [1]. Balises are passive devices, with no external power from the trackside. Most of the time, the balise is in sleep mode. When a train provides an appropriate telepowering signal, it gets activated and generates the Frequency Shift Keying (FSK) signal that carries encoded information. This information includes location information, train operation information, route information, and control data information [2]. It is analyzed by the balise transmission module (BTM) and provided to the on-board control core. The BTS is an indispensable component of the train operation control system [3], presented by Figure 1, playing an essential role in ensuring train position sensing and safe operation [4]. The balise and BTM should be capable of adapting to various operational environments. When a balise is covered by debris, it may not be detected by the BTM due to unsatisfactory matching. The problems caused by debris lead to the loss of transmission performance and further reduce the reliability of the BTS. The loss of balise information during train operation could potentially trigger emergency braking procedures or, in more severe cases, lead to a significant railway incident [5]. Therefore, it is extremely significant to analyze the electromagnetic coupling characteristics of the BTS.

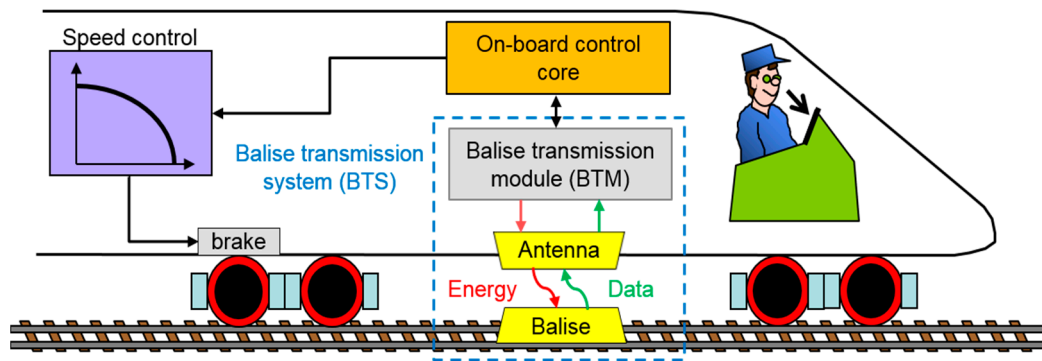


Figure 1. Energy and data transmission of BTS.

In recent years, some scholars have studied the transmission theory of BTS. An electromagnetic coupling model between the onboard antenna unit (OAU) and balise is established by the finite element method. The signal process of the downlink and uplink is simulated [6], and adaptations for reliable transmission of data are analyzed [7]. In [8], the dynamic process of the telepowering signal was analyzed using electromagnetic field theory, and a circuit model for energy conversion of the balise was established. In accordance with the test methodology prescribed by the standard, the relationship between the magnetic field compliance and magnetic field strength was analyzed under various conditions. During high-energy acquisition periods, the dynamic energy harvesting capabilities of the balise were optimized by capping the voltage at a predetermined threshold. The research findings presented in the aforementioned literature primarily focus on the BTS in free space environments. In practice, the BTS operates in extremely challenging environments [9,10], where multiple factors can significantly impact its transmission characteristics [11,12]. These include seasonal elements such as rainwater, ice, and snow; industrial residues such as coal dust and iron; installation variables related to the positioning of a balise on steel rails or wheel guard rails; and vehicle structural issues, particularly the proximity of the OAU to the metallic components beneath the vehicle. These environmental factors not only interfere with the operation of a balise but can also compromise the reliability and efficiency of the BTS. The presence of surrounding debris or metallic objects can significantly impact the performance of the BTS by causing antenna detuning. This phenomenon shifts the antenna's tuning frequency, leading to an increased reflection coefficient and consequent attenuation of the transmitted magnetic field [13]. To counteract these detrimental effects, a practical solution involves installing a metal plate on the rear of the OAU. In order to reduce the system transmission losses, researchers have pursued multiple avenues of investigation focusing on three key areas. First, studies on topology structure compensation aim to optimize the physical layout and arrangement of system components to minimize losses [14,15]. Second, research efforts have been directed towards enhancing oscillator circuit efficiency [16], improving the performance of these crucial components for generating and maintaining signal integrity. Third, investigations into transmission network matching [17–20] seek to optimize impedance matching between various components of the transmission network, thereby reducing signal reflections and maximizing power transfer. Reference [21] presented a low-complexity analytical model for mutual inductance between coupling coils in wireless power transfer systems. The model utilized fundamental data, obtained through three-dimensional electromagnetic numerical simulations, and used a multi-objective genetic programming algorithm for optimization. This approach ensured an optimal balance between accuracy and complexity, enabling the swift and precise evaluation of coil mutual inductance under various misalignment conditions. However, the relative positions of the transmitting and receiving coils in the transmission process of the BTS are variable. The mutual inductance of the coils under driving conditions was numerically simulated, and the compensation network was optimized through the objective function of the resonant circuit [22]. In [23], the effectiveness of voltage-based

calculations in determining the equivalent mutual inductance of multiple coils aligned along the same axis was demonstrated. At a frequency of 13.56 MHz, the method produced simulation values that closely correspond to measured values. The study's experimental approach involved measuring the actual mutual inductance between coils at various distances. The results of these measurements corroborated the consistency between simulated and measured outcomes, validating the reliability of the voltage calculation method.

The electromagnetic coupling process of the BTS under free space conditions has been extensively discussed and analyzed in the literature mentioned above; however, its behavior in complex application environments remains largely unexplored. While the wireless power transmission system shares some similarities with the BTS, research findings from the former are not directly applicable to the latter. This disparity arises primarily from the fact that wireless power transmission systems, predominantly used for device power supply, employ relatively stationary transmitting and receiving antennas, with transmission frequencies typically ranging from a few kHz to several hundred kHz. The frequency range differs significantly from the operating frequency of balises. Moreover, in lossy media, transmission losses far exceed those of wireless power supply systems. Additionally, when a train passes a balise, the relative position varies with the train's location, unlike that of wireless power supply systems. The transmission characteristics in water debris are one influential factor. It is difficult to accurately estimate the effect of the medium on the transmission characteristics when the balise is immersed in water. Consequently, it is necessary to establish a circuit model to analyze the transmission characteristics of the BTS. In response to the application of the BTS for underwater debris, this paper proposes a modeling method for the BTS using S-parameters. Utilizing the electromagnetic analysis and two-port network analysis, we can derive an equivalent circuit of the BTS with the frequency and conductivity of water debris taken into consideration. In this paper, measurements, simulations, and theoretical calculations have been implemented using the proposed equivalent circuit for a variety of positions between the OAU and the balise. Additionally, we analyze the power differential of the balise uplink signal in water debris environments compared to free space conditions.

The remaining sections of this paper are organized as follows: In Section 2, an electrical model for the BTS in free space is established. Section 3 analyzes the magnetic field strength and transmission impedance for underwater debris. Section 4 presents the validation of the proposed electrical model through instruments and analyzes the transmission parameter characteristics that are actually measured. Section 5 provides a comprehensive discussion of the findings and presents the conclusions of this study.

2. Electrical Modeling of BTS in Free Space

The BTS comprises the uplink FSK signal channel and downlink telepowering signal channel. It facilitates the bidirectional wireless transmission of energy and information via an alternating electromagnetic field generated between the OAU and the balise. In free space conditions, the medium is considered non-conductive. The center frequency of the uplink signal is 4.234 MHz. The present study focuses on the uplink signal transmission process of the balise as a representative case for subsequent analysis.

2.1. Electromagnetic Coupling Model

In the BTS, the OAU and balise antenna are approximately rectangular. The specifications [24] constrain the electrical dimensions of the balise, with the antenna model measuring 390 mm in length and 200 mm in width. When the antenna perimeter l satisfies the relationship expressed in Equation (1) with the signal wavelength λ , it can be assumed that the current distribution on both antennas is uniform, with equal amplitude and direction at all points.

$$l < \frac{\lambda}{2\pi} \quad (1)$$

Figure 2 illustrates a three-dimensional Cartesian coordinate system (xyz) established with the center of the balise designated as the origin O . Rectangle $ABCD$ depicts the balise,

while rectangle $EFGH$ represents the OAU. Point P indicates the electrical center of the OAU. The balise is installed in the middle of the track, the position is unchanged, and the OAU is moved. Rectangles $E_1F_1G_1H_1$ and $E_2F_2G_2H_2$ represent the relative positions of the OAU with respect to the balise at two distinct time points. The train speed velocity vector \vec{v} aligns with the positive direction of the Ox axis. The relative height between the OAU and the balise is h . The magnetic flux density generated by the balise at any point P_1 within the OAU can be expressed by Equation (2):

$$B = \frac{\mu I}{4\pi} \oint_C \left(\frac{d\vec{l} \times \vec{r}}{r^3} \right) \quad (2)$$

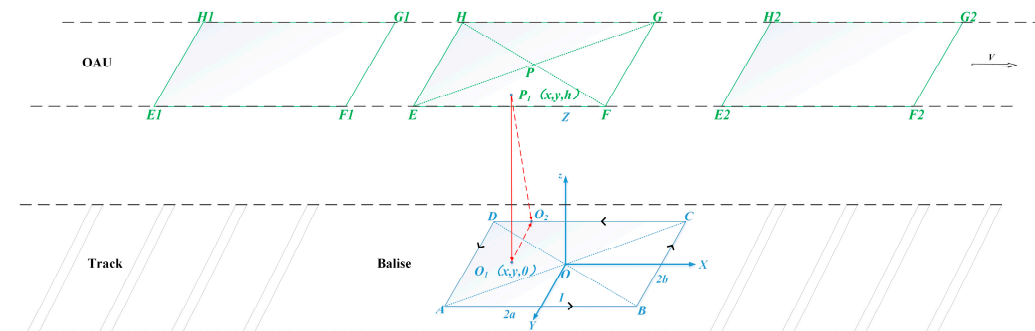


Figure 2. Schematic diagram of electromagnetic coupling model between OAU and balise.

In the equation, I represents the current of the transponder antenna, C denotes the curve formed by rectangle $ABCD$, $Id\vec{l}$ represents the current element, and \vec{r} denotes the vector distance from any point P_1 to the current element. Let the length of side AB of rectangle $ABCD$ be $2a$, the length of side CD be $2b$, the length of side EF of rectangle $EFGH$ be $2c$, and the length of side GH be $2d$. Point O_1 is the projection of point P_1 on plane $ABCD$, and P_1O_2 is perpendicular to line CD . The magnetic flux density generated by the balise along the Z -axis at point P_1 can be expressed by Equation (3):

$$B_z = B_{zAB} + B_{zBC} + B_{zCD} + B_{zDA} = I \cdot N(a, b, \mu, x, y, h) \quad (3)$$

$$N(a, b, h, \mu, x, y) = \frac{\mu}{4\pi} \left\{ \begin{aligned} & \frac{b+y}{(b+y)^2+h^2} \cdot \left[\frac{a+x}{\sqrt{(a+x)^2+(b+y)^2+h^2}} + \frac{a-x}{\sqrt{(a-x)^2+(b+y)^2+h^2}} \right] \\ & + \frac{a+x}{(a+x)^2+h^2} \cdot \left[\frac{b+y}{\sqrt{(a+x)^2+(b+y)^2+h^2}} + \frac{b-y}{\sqrt{(a+x)^2+(b-y)^2+h^2}} \right] \\ & + \frac{b-y}{(b-y)^2+h^2} \cdot \left[\frac{a+x}{\sqrt{(a+x)^2+(b-y)^2+h^2}} + \frac{a-x}{\sqrt{(a-x)^2+(b-y)^2+h^2}} \right] \\ & + \frac{a-x}{(a-x)^2+h^2} \cdot \left[\frac{b+y}{\sqrt{(a-x)^2+(b+y)^2+h^2}} + \frac{b-y}{\sqrt{(a-x)^2+(b-y)^2+h^2}} \right] \end{aligned} \right\}$$

Then, the magnetic flux received by the OAU φ can be expressed by Equation (4):

$$\varphi = \int_{-c}^c \int_{-d}^d B_z dx dy = I \cdot \int_{-c}^c \int_{-d}^d N(a, b, h, \mu, x, y) dx dy \quad (4)$$

Derive Equation (5) based on the relationship between the magnetic flux and mutual inductance.

$$M(a, b, h, \mu, x, y) = \int_{-c}^c \int_{-d}^d N(a, b, h, \mu, x, y) dx dy \quad (5)$$

When a train provides an appropriate telepowering signal, the voltage U of the received signal on the OAU can be approximated as the electromotive force induced at that position when the train is stationary [25]. Q represents the quality factor of the resonant circuit, ω denotes the angular frequency, and the formula for calculating U is as follows:

$$U = -j\omega n\phi Q = -j\omega nIQM(a, b, h, \mu, x, y) \quad (6)$$

According to these relationships, the voltage of the OAU is related to the number of turns n , the mutual inductance M , and the current I of the balise. The mutual inductance M is further influenced by the dimensions, relative positions, and transmission medium characteristics of the OAU and the balise.

2.2. Circuit Modeling Analysis

To optimize the transmission of uplink FSK signals and reduce the potential for signal distortion that can occur due to reflections, it is standard practice to implement impedance matching between the OAU and the balise. This impedance matching approach is crucial for maintaining the signal integrity and ensuring reliable communication. The equivalent circuit diagram representing the antenna configuration for uplink FSK signal transmission is shown in Figure 3. This circuit utilizes a π -type matching network, which is a common and effective method for achieving the desired impedance match [26]. The π -type matching network consists of passive components, allowing for the flexible adjustment of impedance characteristics to optimize signal transfer between the OAU and balise components of the system.

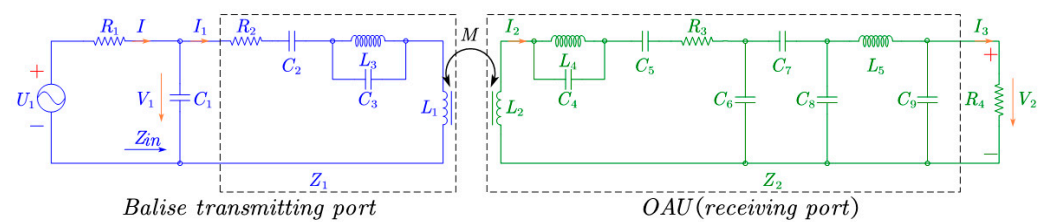


Figure 3. Equivalent circuit of uplink FSK signal.

In the uplink FSK signal chain of the BTS, U_1 represents the equivalent voltage source at the transmitting port, I denotes the total current in the balise antenna, V_1 signifies the voltage across the transmission channel, and V_2 indicates the voltage across the load R_4 . Z_{in} stands for the input impedance of the transmitting port, while Z_1 represents the transmitting antenna impedance. R_1 is the equivalent resistance of the transmitting circuit. C_1 – C_3 and L_3 are the capacitors and inductor, respectively, used for tuning and matching at the transmitting port. L_1 represents the equivalent inductance of the balise antenna, R_2 denotes the sum of the balise antenna's equivalent resistance and the series loss resistance, and I_1 is the current flowing through the balise antenna. For the OAU port, Z_2 represents the impedance of the receiving antenna, L_2 represents the equivalent inductance of the receiving antenna, and I_2 is the induced current in the antenna. R_3 is the sum of the antenna's equivalent resistance and the series loss resistance. C_4 – C_6 and L_4 are the capacitors and inductor for tuning and matching at the receiving port. C_7 – C_9 and L_5 form a composite π -type impedance matching network, which can filter the telepowering signals of the downlink. C_8 and C_9 are variable capacitors to adapt to mismatches introduced during transmission under various environmental conditions. I_4 is the current flowing through the load impedance R_4 . Z_{11} and Z_{22} represent the total impedance of the balise transmitting port and the OAU receiving port. M is the mutual inductance between the OAU and the balise.

In Figure 3, Z_1 represents the series branch impedance of the balise port, with Z_{11} and Z_1 expressed by Equation (7). Z_2 denotes the parallel load impedance of the OAU receiving port, with Z_{22} and Z_2 expressed by Equation (8).

$$\begin{cases} Z_{11} = R_1 + \frac{Z_1}{1+Z_1j\omega C_1} \\ Z_1 = \frac{j\omega L_3}{1-\omega^2 C_3 L_3} + \frac{1}{j\omega C_2} + j\omega L_1 + R_2 \end{cases} \quad (7)$$

$$\begin{cases} Z_{22} = \frac{Z'_2 + j\omega L_5}{1 + (j\omega C_9 + \frac{1}{R_4})(Z'_2 + j\omega L_5)} \\ Z_2 = \frac{Z'_2 + j\omega L_5}{1 + j\omega C_9(Z'_2 + j\omega L_5)} \end{cases} \quad (8)$$

In Equation (8), Z'_2 is derived from the circuit structure and is expressed by Equation (9).

$$Z'_2 = \frac{(j\omega L_2 + \frac{j\omega L_4}{1-\omega^2 C_4 L_4} + \frac{1}{j\omega C_5} + R_3)(j\omega C_6 + j\omega C_7) + 1}{(j\omega C_7 + j\omega C_8)(1 - \omega^2 C_6 L_2 + \frac{\omega^2 C_6 L_4}{\omega^2 C_4 L_4 - 1} + \frac{C_6}{C_5} + R_3 j\omega C_6) - \omega^2 C_7 C_8(j\omega L_2 + \frac{j\omega L_4}{1-\omega^2 C_4 L_4} + \frac{1}{j\omega C_5} + R_3)} \quad (9)$$

According to KCL, the relationship between currents I and I_1 can be expressed as

$$I = \left(1 + Z_1 j\omega C_1 + \frac{j\omega^3 M^2 C_1}{Z_{22}}\right) I_1 \quad (10)$$

Combining Equations (7), (8) and (10), the equivalent circuit voltage equation for the OAU and the balise in Figure 3 can be expressed as:

$$\begin{cases} (R_1 + R_1 Z_1 j\omega C_1 + \frac{j\omega^3 M^2 R_1 C_1}{Z_{22}} + Z_1) I_1 - j\omega M I_2 = U_1 \\ -j\omega M I_1 + \frac{(Z'_2 + j\omega L_5) I_2}{1 + (j\omega C_9 + \frac{1}{R_4})(Z'_2 + j\omega L_5)} = 0 \end{cases} \quad (11)$$

The parameters of the inductors and capacitors in the circuit are designed based on the operating resonant frequency of the BTS. Given that the antenna exhibits inductive behavior at the operating frequency, the inductance values of antennas L_1 and L_2 should be considered during impedance matching. When the antenna frequency is 4.234 MHz, the sum of the imaginary part at the transmitting port $j\omega R_1 Z_1 C_1 + j\omega^3 M^2 R_1 C_1 Z_{22}^{-1} + Z_1$ is approximated as 0, and the real part is approximated as R_2 . For the receiving port, the sum of the imaginary part $(Z'_2 + j\omega L_5) \left[1 + (j\omega C_9 + \frac{1}{R_4})(Z'_2 + j\omega L_5)\right]^{-1}$ is approximated as 0, and the real part is approximated as $R_3 + R_4$. Therefore, the relationship between voltages V_1 , V_2 , and impedance Z_{in} can be expressed as:

$$\begin{cases} V_1 = I_1 R_2 - j\omega M I_3 \\ V_2 = -I_3 R_3 + j\omega M I_1 \end{cases} \quad (12)$$

$$Z_{in} = R_2 - j\omega M \frac{I_3}{I_1} \quad (13)$$

When the balise transmitting power is P , the current I_1 in the balise and the current I_3 in the load of the OAU satisfy the relationship expressed in Equation (14).

$$\begin{cases} P = \frac{U_1^2}{R_1} \\ I_1 = \frac{U_1}{R_1 + Z_{in}} \\ I_3 = \frac{V_2}{R_4} \end{cases} \quad (14)$$

Equations (12) and (14) can be respectively substituted into Equation (13) to derive the relationship between mutual inductance M and load voltage V_2 , so:

$$j\omega M = \frac{V_2 + I_2 R_3}{I_1} = \frac{V_2(R_1 + Z_{in})\left(1 + \frac{R_3}{R_4}\right)}{\sqrt{R_1 P}} \quad (15)$$

Substituting Equation (5) into Equation (15) enables the derivation of the relationship expression for the voltage V_2 across the load.

$$V_2 = \frac{j\omega\sqrt{R_1 P} \int_{-c}^c \int_{-d}^d N(a, b, h, \mu, x, y) dx dy}{(R_1 + Z_{in})\left(1 + \frac{R_3}{R_4}\right)} \quad (16)$$

From Equation (16), it can be observed that after proper circuit matching, the voltage of the load is influenced by the dimensions of the OAU and the balise, their relative spatial positions, and the input power of the balise. However, it is independent of the reactive components in the matching circuit. The load at the receiving port of the OAU needs to effectively utilize the available power transmitted from the balise. In order to describe the transmission characteristics of the BTS, the insertion loss parameter is used. The calculation formula is as follows:

$$S_{21}(dB) = 20\log_{10} \left| \frac{\omega \int_{-c}^c \int_{-d}^d N(a, b, h, \mu, x, y) dx dy}{R_1} \right| + 20\log_{10}(\alpha) \quad (17)$$

where $\alpha = \left(1 + Z_{in}R_1^{-1}\right)\left(1 + R_3R_4^{-1}\right)$.

According to Equation (17), when debris is present near the OAU and the balise, both the mutual inductance M of the BTS and the input impedance Z_{in} are changed, resulting in alterations in the transmission characteristics.

3. Electromagnetic Modeling of Balise for Underwater Debris

When the balise uplink FSK signal penetrates conductive media, it generates an electric field that suppresses changes in the magnetic field. Due to the conductivity of water, eddy currents are produced, resulting in additional power loss. Moreover, as the uplink FSK signal frequency is 4.234 MHz, the eddy current loss in water media can no longer be disregarded [27]. Consequently, the calculation and analysis of eddy current loss become crucial.

3.1. Magnetic Field Strength of Conductive Media

Some studies on electromagnetic coupling in conductive media have been conducted using electromagnetic field analysis. Most of them are based on circular coil models, assuming the coils are fully immersed in water for calculations and analysis [28,29]. However, the OAU and the balise are approximately rectangular, with the magnetic field primarily concentrated in the main lobe zone. Therefore, electromagnetic field analysis is performed for the main lobe zone in the presence of conductive media.

As shown in Figure 4, the balise ABCD is composed of four finite-length conductors, with a cavity of height h_0 above it. Regions 0 and 2 are free space, while region 1 is dielectric water. The electrical conductivity, dielectric constant, and magnetic permeability of each region are denoted by σ_i , ϵ_i , and μ_i . The three regions are analyzed separately, assuming the medium in each region is linear, homogeneous, and isotropic.

For region 0, $z < 0$, and the magnetic field coexists with the reflected magnetic field generated by eddy currents in this area. Assuming the current density of the balise is J , the magnetic vector potential A_0 at any point (x, y, h) in the free space above it can be expressed as:

$$A_0(x, y, h) = \frac{\mu_0}{4\pi} \int_v \frac{J(x', y', z') dv'}{r} \quad (18)$$

$$B_0 = \nabla \times A_0 \quad (19)$$

where J represents the current density of the balise, dv' represents the elementary volume of the source, and r is the distance between any point (x, y, h) and a point source (x', y', z') on the balise. The distance r can be expressed as:

$$r = \sqrt{(x - x')^2 + (y - y')^2 + (h - z')^2} \quad (20)$$

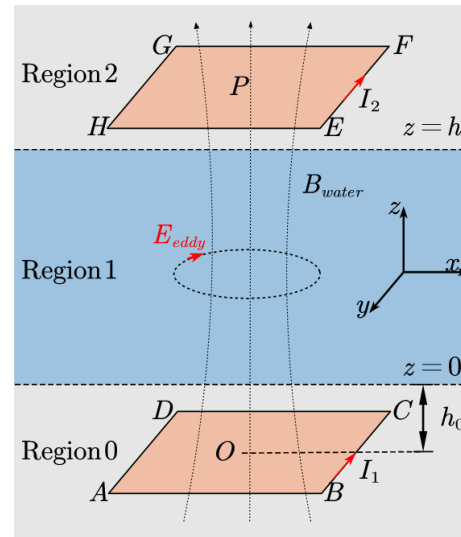


Figure 4. Electromagnetic coupling for underwater debris.

Considering that no eddy currents exist in this region, the formula for calculating the reflected magnetic flux density B_r is as follows:

$$\nabla^2 B_r = 0 \quad (21)$$

$$\nabla \times B_r = 0 \quad (22)$$

For region 1, $0 < z < h$, and the magnetic flux density B_1 is given by:

$$\nabla^2 B_1 - (\omega^2 \mu_1 \epsilon_1 - j\omega \mu_1 \sigma_1) B_1 = 0 \quad (23)$$

$$\nabla \cdot B_1 = 0 \quad (24)$$

For region 2, $h < z$, and the magnetic flux density B_2 is given by:

$$\nabla^2 B_2 = 0 \quad (25)$$

$$\nabla \cdot B_2 = 0 \quad (26)$$

To solve the aforementioned equation, we introduce the method of double Fourier transform [30,31] and its inverse transform as follows:

$$b(\xi, \eta, z) = \int_{-\infty}^{\infty} \int_{-\infty}^{\infty} B(x, y, z) e^{-j(x\xi + y\eta)} dx dy \quad (27)$$

$$B(x, y, z) = \frac{1}{4\pi^2} \int_{-\infty}^{\infty} \int_{-\infty}^{\infty} b(\xi, \eta, z) e^{j(x\xi + y\eta)} d\xi d\eta \quad (28)$$

where ξ and η are integration variables used in the double Fourier transform. The normal component of the magnetic flux density and the tangential component of the magnetic

field strength remain continuous across the boundary interface. The following relationship holds true:

$$\begin{cases} b_{iz} + b_{rz} = b_{1z}, & z = 0; \\ \mu_1(b_{ix} + b_{rx}) = \mu_0 b_{1x}, & z = 0; \\ b_{1z} = b_{2z}, & z = h; \\ \mu_2 b_{1x} = \mu_1 b_{2x}, & z = h; \end{cases} \quad (29)$$

Considering that the magnetic flux density at infinity is 0, the Z-axis component B_{2z} of the magnetic flux density from the balise to the OAU is:

$$B_{2z}(x, y, z) = \frac{\mu_0 I_1}{2\pi^2} \int_{-\infty}^{\infty} \int_{-\infty}^{\infty} \frac{k \delta \sin(a\xi) \sin(b\eta)}{\xi \eta} e^{-k(z+h_0)} e^{-j(x\xi+y\eta)} d\xi d\eta \quad (30)$$

In Equation (30), regions 0 and 2 comprise the same medium, with magnetic permeability μ_0 . Where δ , k , and γ_1 can be expressed as follows:

$$\delta = \frac{4\mu_0 \mu_1 k \gamma_1 e^{(k+\gamma_1)h}}{(\mu_0 \gamma_1 + \mu_1 k)^2 e^{2\gamma_1 h} - (\mu_0 \gamma_1 - \mu_1 k)^2} \quad (31)$$

$$k = \sqrt{\xi^2 + \eta^2} \quad (32)$$

$$\gamma_1 = \sqrt{\omega^2 \mu_1 \varepsilon_1 - j\omega \mu_1 \sigma_1} \quad (33)$$

When the center P of the OAU is at (P_x, P_y, h) , according to Equation (4), the magnetic flux φ_{water} received by the antenna is:

$$\begin{aligned} \varphi_{water} &= \int_{P_y-d}^{P_y+d} \int_{P_x-c}^{P_x+c} B_{2z}(x, y, h) dx dy \\ &= \frac{2\mu_0 I_1}{\pi^2} \int_{-\infty}^{\infty} \int_{-\infty}^{\infty} \frac{k \delta}{\xi^2 \eta^2} \sin(a\xi) \sin(b\eta) \sin(c\xi) \sin(d\eta) e^{-k(h+h_0)} e^{-j(P_x \xi + P_y \eta)} d\xi d\eta \end{aligned} \quad (34)$$

Combining Equations (5) and (34), the mutual inductance M_{water} between the OAU and the balise for underwater debris can be expressed as:

$$M_{water} = \frac{8\mu_0}{\pi^2} \int_0^{\infty} \int_0^{\infty} \frac{k \delta}{\xi^2 \eta^2} \sin(a\xi) \sin(b\eta) \sin(c\xi) \sin(d\eta) \cos(P_x \xi + P_y \eta) e^{-k(h+h_0)} d\xi d\eta \quad (35)$$

Equation (35) represents a crucial parameter for quantitatively evaluating the electromagnetic coupling characteristics of underwater transponders. In conjunction with Equation (6), the voltage U_{water} received by the OAU is derived as:

$$U_{water} = -j\omega n Q \varphi_{water} = \frac{8n\omega \mu_0 I_1}{j\pi^2} \int_0^{\infty} \int_0^{\infty} \frac{k \delta}{\xi^2 \eta^2} \sin(a\xi) \sin(b\eta) \sin(c\xi) \sin(d\eta) \cos(P_x \xi + P_y \eta) e^{-k(h+h_0)} d\xi d\eta \quad (36)$$

3.2. Impedance Analysis of Transmission Circuits

To obtain an effective circuit model, it is essential to analyze the impedance variations of the OAU and the balise for underwater debris. The conductive medium is equivalent to a circuit with specific impedance characteristics [32]. By turning the capacitors C8 and C9 in Figure 3, the OAU and the balise transmission circuit can achieve optimal matching for underwater debris. Figure 5 illustrates the two-port network of the BTS.

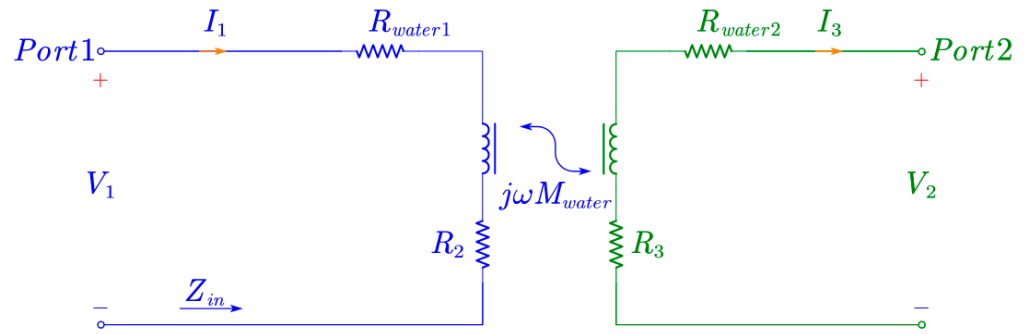


Figure 5. Dual-port coupled network for underwater debris.

In Figure 5, R_2 and R_3 represent the equivalent impedance of the antenna in free space, and changes in the underwater environment can be disregarded [33]. R_{water1} and R_{water2} denote the radiation resistance in the underwater debris [28,34], which can be expressed as:

$$R_{water} = \frac{\omega\mu_1}{4\pi} \iint \frac{e^{-\omega\mu_1\sigma_1 r}}{r} \sin(\omega\mu_1\sigma_1) r \cos\psi ds_1 ds_2 \quad (37)$$

In the equation, r represents the distance from the balise to any point source on the OAU, while ψ denotes the vector angle between two point sources. As is evident from Equations (35) and (37), the radiation resistance R_{water} and mutual inductance M_{water} of the balise are related to the frequency and electrical conductivity of the transmission medium. Accordingly, the input impedance Z_{in_water} for underwater debris can be calculated as:

$$Z_{in_water} = \frac{V_{water1}}{I_{water1}} = R_2 + R_{water1} + \frac{(\omega M_{water})^2}{R_3 + R_{water2}} \quad (38)$$

According to Equation (17), by substituting the expressions for input impedance Z_{in_water} and mutual inductance M_{water} , the S21 parameter of the BTS for underwater debris can be calculated. When the OAU and balise performance parameters remain constant, the insertion loss of the BTS for underwater debris is related to the input impedance Z_{in_water} and mutual inductance M_{water} . As the input impedance at different positions can be measured in real time using the circuit model [35], the evaluation of the BTS performance can be achieved through the mutual inductance M .

4. Simulation Analysis and Measurement Verification

In this section, the proposed electromagnetic coupling model is implemented and measured to compare with the theoretical calculated results and electromagnetic simulation results in the main lobe zone. Referencing the relative position in the specifications [24], we analyze the mutual inductance parameters between the OAU and the balise, the equivalent impedance of the circuit network, and transmission loss characteristics. The influence of the conducting medium on the S21 parameters is analyzed, and the I/O characteristics of the balise in underwater debris are predicted. In addition, experiments are carried out to validate the comparison of the I/O characteristics in free space and with underwater debris.

4.1. Simulation Analysis and Verification of Mutual Inductance

In this section, the transmission characteristics of the balise uplink FSK signal are used as an example to validate the mutual inductance of the circuit model in free space and water debris. The simulation is conducted using Comsol 5.6, with a magnetic permeability of $4\pi \times 10^{-7}$ H/m. The experiment is carried out on a non-magnetic acrylic framework, as shown in Figure 6. The OAU and balise are both designed with dimensions of 390 mm × 200 mm in length and width. A network analyzer is employed to measure the transmission parameters, with the frequency set to 4.234 MHz.

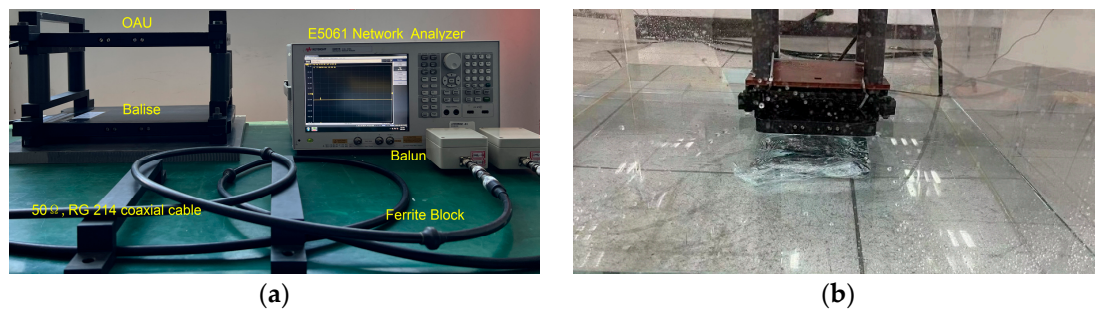


Figure 6. Measurement experiment system of mutual inductance; (a) Free space; (b) Water debris.

To maintain consistency with practical engineering, both the simulation and experimental processes keep the balise stationary, while the relative position changes are achieved by moving the OAU. They are made of copper and have identical dimensions, with a length and width of $2a = 2c = 390$ mm and $2b = 2d = 200$ mm. When the OAU and the balise are in different installation scenarios, their relative vertical distance h varies accordingly. As the OAU moves along the Z-axis with a step size of 30 mm, and the vertical distance h between the geometric centers of the OAU and the balise increases from 220 mm to 460 mm, the mutual inductance variation curves for free space and underwater debris are shown in Figure 7.

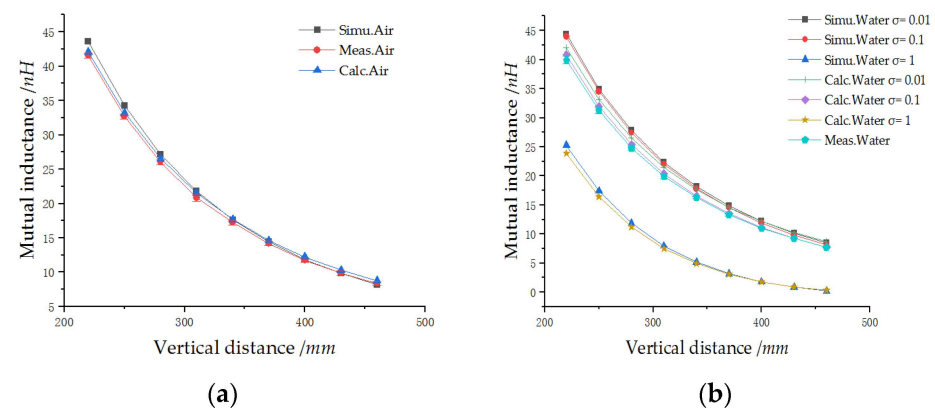


Figure 7. Mutual inductance variation curve versus vertical displacement; (a) Free space (air); (b) Water debris (water).

In Figure 7, the mutual inductance between the OAU and the balise gradually decreases as the vertical distance increases in free space and water debris. Due to the coupling magnetic flux between the two antennas diminishing with increased distance, the mutual inductance is reduced. In water debris, as the electrical conductivity σ increases, the mutual inductance between the OAU and the balise decreases. The discrepancy between the experimentally determined mutual inductance measurements and the values obtained through theoretical calculations and computer simulations is minimal. The calculated results are generally consistent with simulation and experimental findings.

Figure 8 shows the mutual inductance variation curves corresponding to the X-axis horizontal offsets. The vertical distances between the OAU and the balise are selected as 220 mm, 340 mm, and 460 mm. When the vertical distance h is 220 mm, horizontal offsets occur in 25 mm increments, with the offset Δx increasing from 0 mm to 250 mm. When h is 340 mm, horizontal offsets occur in 30 mm increments, with Δx increasing from 0 mm to 300 mm. When h is 460 mm, horizontal offsets occur in 35 mm increments, with Δx increasing from 0 mm to 350 mm. Under all three height conditions, the mutual inductance decreases as the horizontal offset Δx increases. This is primarily due to the reduction in the overlapping area between the OAU and the balise as Δx increases, leading to the magnetic flux between the antennas being reduced. As the conductivity σ increases, the mutual inductance between the two antennas decreases. As shown in the figure, the deviation

between the measured mutual inductance values and those obtained through theoretical calculations and simulations varies within a narrow range, demonstrating excellent overall consistency. Notably, as the central positions of the two reference loops gradually move apart, the relative deviation gradually increases. This is primarily due to the decrease in mutual inductance with distance. However, considering the operational range of the balise, the model's results remain valid for our purposes.

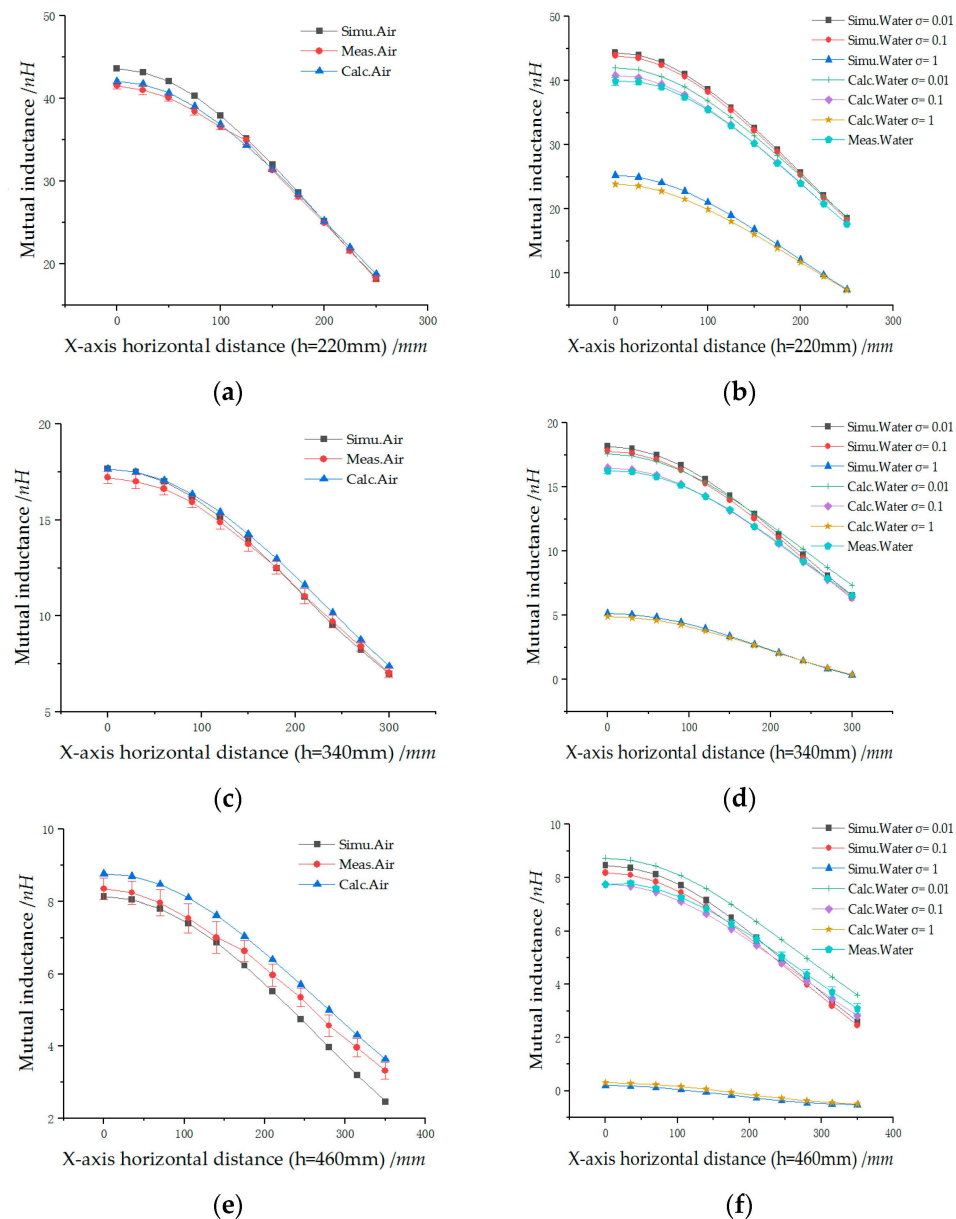


Figure 8. Mutual inductance variation curve versus X-axis horizontal displacement; (a) Free space (air, $h = 220$ mm); (b) Water debris (water, $h = 220$ mm); (c) Free space (air, $h = 340$ mm); (d) Water debris (water, $h = 340$ mm); (e) Free space (air, $h = 460$ mm); (f) Water debris (water, $h = 460$ mm).

Figure 9 shows the mutual inductance variation curves corresponding to the Y-axis horizontal offsets. The vertical distances between the OAU and the balise are selected as 220 mm, 340 mm, and 460 mm. When the vertical distance h is 220 mm, horizontal offsets occur in 25 mm increments, with the offset Δy increasing from 0 mm to 250 mm. When h is 340 mm, Y-axis offsets occur in 30 mm increments, with Δy increasing from 0 mm to 300 mm. When h is 460 mm, Y-axis offsets occur in 35 mm increments, with Δy increasing from 0 mm to 350 mm. Similar to the X-axis direction, under all three height

conditions, the mutual inductance decreases as the horizontal offset Δy increases. This is primarily due to the reduction in the overlapping area between the OAU and the balise as Δy increases, leading to reduced magnetic flux between the antennas. However, compared to the X-axis direction, the decrease in mutual inductance is more rapid along the Y-axis, as Y-axis changes result in a greater reduction of the relative overlapping area. As the conductivity σ increases, the mutual inductance between the two antennas decreases. The measured mutual inductance values closely align with the theoretical calculations and simulations, exhibiting only minor deviations. As the reference loops' central positions diverge, the relative deviation increases slightly, primarily due to the inverse relationship between the mutual inductance and distance. However, the model's results remain valid within the balise's operational range.

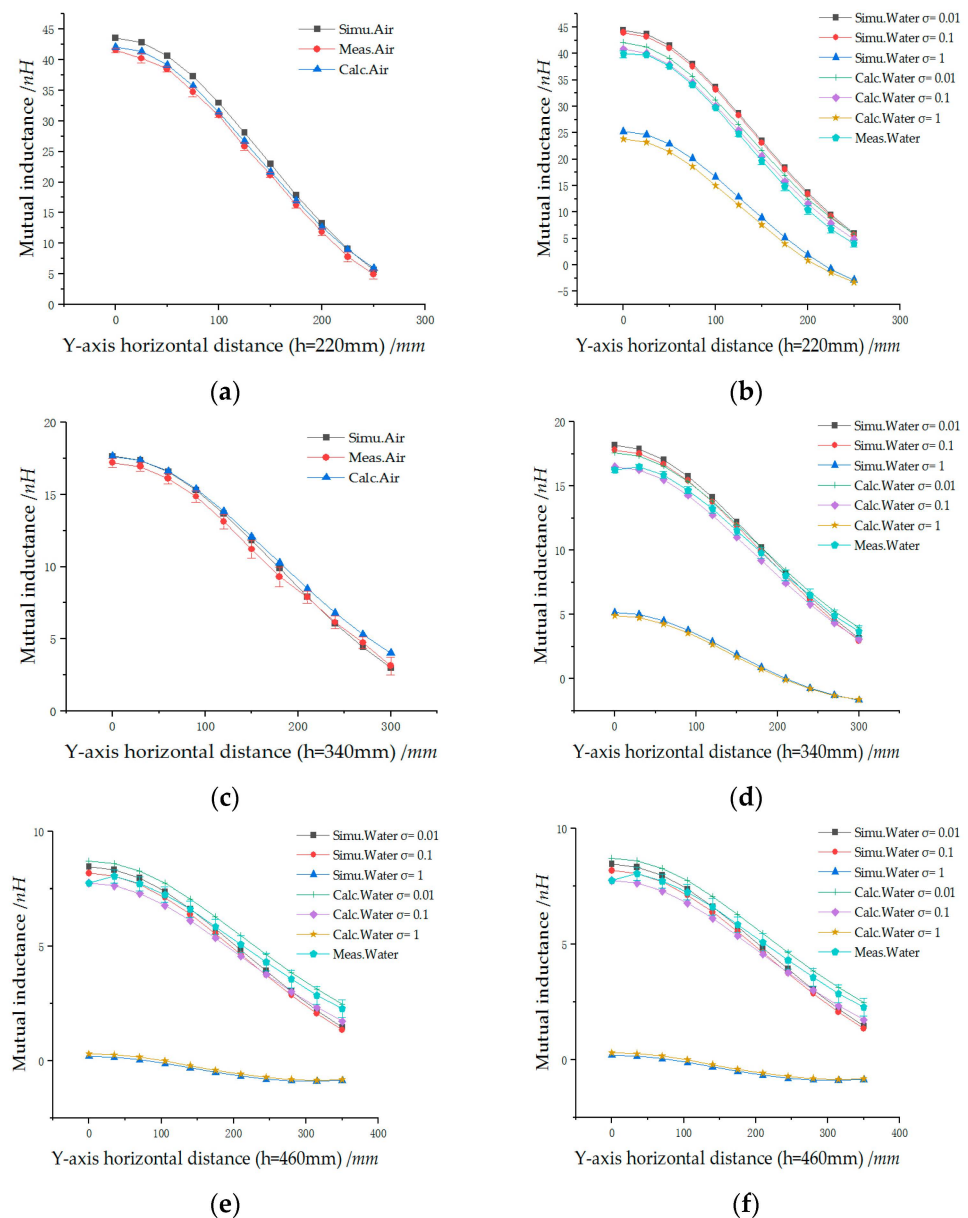


Figure 9. Mutual inductance variation curve versus Y-axis horizontal displacement; (a) Free space (air, $h = 220$ mm); (b) Water debris (water, $h = 220$ mm); (c) Free space (air, $h = 340$ mm); (d) Water debris (water, $h = 340$ mm); (e) Free space (air, $h = 460$ mm); (f) Water debris (water, $h = 460$ mm).

4.2. Transmission Loss Analysis

When the BTS works, its performance is influenced by the transmission medium. The uplink transmission loss variations are studied in both free space and water debris. Based on the analysis results shown in Figures 7–9, an electrical conductivity of $\sigma = 0.1$ S/m is selected for transmission loss analysis in water debris. In the experiment, the number of turns is $n = 1$, the network analyzer port resistances are $R_1 = R_4 = 50 \Omega$, the antenna equivalent resistances are $R_2 = R_3 = 0.1 \Omega$, and the cavity thickness h_0 is 5 mm.

Figure 10 shows the S21 parameter corresponding to vertical movement along the z-axis. As the perpendicular distance between the OAU and the balise increases from 220 mm to 460 mm, S21 gradually increases, indicating greater transmission loss. The transmission attenuation in water debris is greater than that in free space, and the calculated results are largely consistent with the experimental results. The data points below the graph indicate the deviation between the measured results and calculated results at various heights in free space, with a maximum deviation of 0.34 dB. The values above show the deviation in water debris, with a maximum of 0.21 dB.

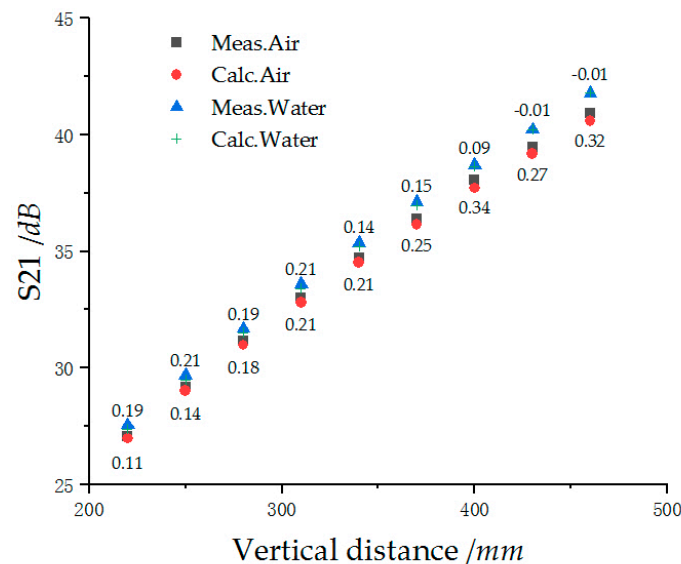


Figure 10. S21 parameter variation curve versus vertical displacement.

In Figure 11, it can be observed that the S21 parameter of the uplink FSK signal in the BTS gradually increases as the relative horizontal distance grows, indicating greater signal attenuation. The attenuation rate of the S21 parameter in the Y-axis direction is faster than that in the X-axis direction, owing to the fact that changes along the Y-axis lead to greater variations in the relatively overlapping area between antennas. The calculated results are generally consistent with the experimental findings. In free space, the maximum attenuation deviation along the X-axis is 0.38 dB, while along the Y-axis, it is 0.49 dB. In water debris, the maximum attenuation deviation along the X-axis is 0.35 dB, and along the Y-axis, it is 0.39 dB. The S21 parameter's maximum relative deviation closely aligns with the inductance's relative error trend, demonstrating a strong correlation between these key metrics. Given the operational range of the balise, the model's results remain valid for our purposes.

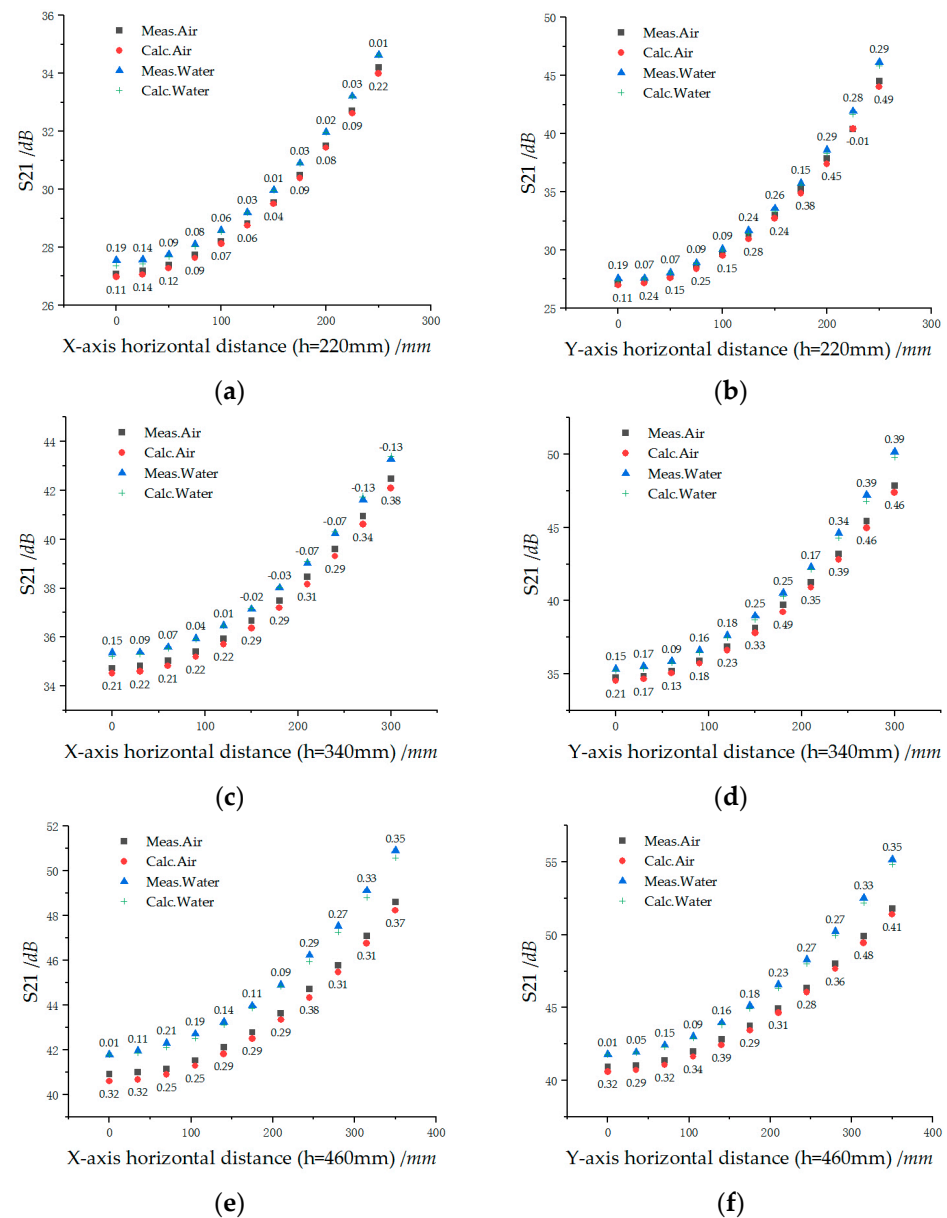


Figure 11. S21 parameter variation curve versus horizontal displacement; (a) X-axis ($h = 220$ mm); (b) Y-axis ($h = 220$ mm); (c) X-axis ($h = 340$ mm); (d) Y-axis ($h = 340$ mm); (e) X-axis ($h = 460$ mm); (f) Y-axis ($h = 460$ mm).

4.3. Analysis of Balise I/O Characteristics

To characterize the relationship between the uplink FSK signal transmission current intensity and the magnetic flux intensity of the received downlink telepowering signal in the BTS, the electrical model of the balise I/O characteristics is verified according to the current specification [24]. Figure 12 illustrates the test system used for this verification, comprising a core control unit, an excitation unit, and an acquisition unit.

In Figure 12, the excitation unit comprises a signal generator (NI-PXIe 5451), a power amplifier (E&I 325LA), two attenuators (Attenuator A: 6 dB 20 W, Attenuator B: 3 dB 100W), and custom-made components (balun and transmitting antenna). The acquisition unit consists of a vector signal analyzer (NI-PXI 5661), a power meter (RS-NRVD), a low-pass filter (Mini Circuits, BLP-10.7), and custom-made components (balun and receiving antenna). The custom-made balun, transmitting antenna, and receiving antenna collectively form the test antenna. The two channels of the vector signal analyzer and power meter are used to measure the voltage of the 4.234 MHz uplink FSK signal and the power of the

27.095 MHz downlink telepowering signal. The core control unit (NI-PXIE 8135) is used for instrument control and data analysis. All modules of the test system are designed based on the ETCS SUBSET-085 specification. When a train provides an appropriate telepowering signal, the loop current in the balise is determined by the received magnetic flux and the mutual inductance of the BTS. Table 1 shows the relevant parameter requirements for the balise as specified in ETCS SUBSET-036, which defines the upper and lower limits of the balise I/O characteristics.

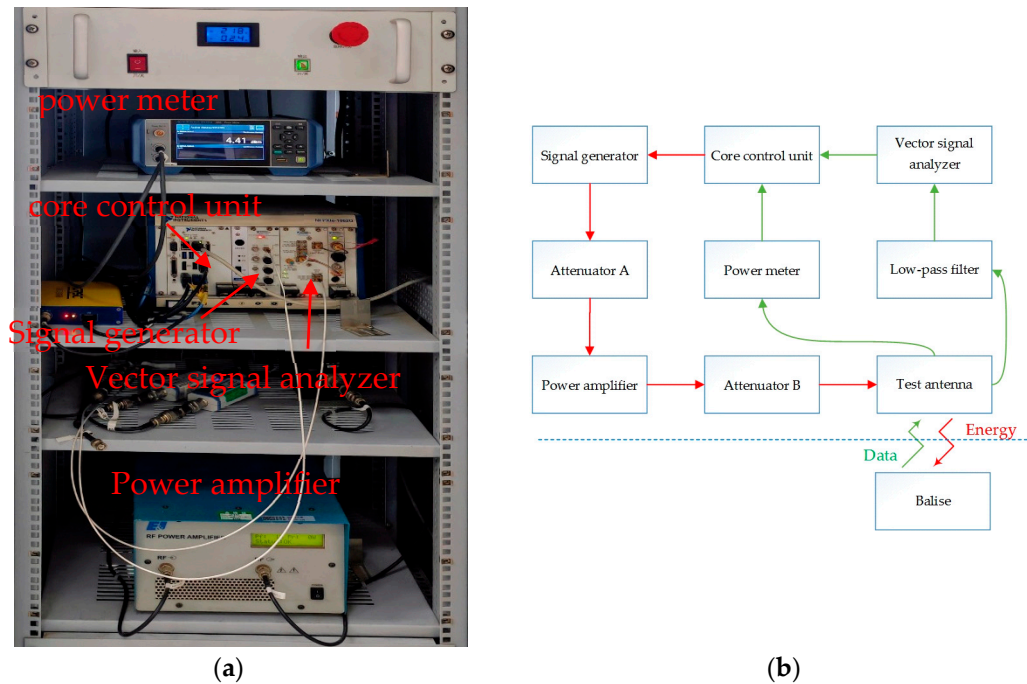


Figure 12. Schematic diagram of the connection relationship; (a) Instruments for I/O characteristics measurements; (b) Test set-up for I/O characteristics measurements.

Table 1. I/O transfer characteristics for a balise.

Telepowering Magnetic Flux (nVs)	Loop Current (mA)
$\varphi_{d1} = 4.9$	$I_{u1} = 37$
$\varphi_{d2} = 7.7$	$I_{u2} = 59$
$\varphi_{d3} = 5.8$	$I_{u3} = 186$
$\varphi_{d4} = 130$	$I_{u4} = 186$

The measurements start with the lowest flux, and with increasing flux, will reach φ_{d4} ; then, the flux is decreased again to the lowest flux. In this experiment, we configure the NI-PXIE 5451 to 27.095 MHz in CW mode. The test antenna is positioned at a height of 220 mm relative to the balise. We adjust the amplitude of NI-PXIE 5451 to achieve the desired power level and record the value. We then measure and record the 4.2 MHz power level. Using these measurements, we calculate the flux and balise loop current. This process is repeated for all flux levels.

The balise is measured in accordance with the specifications. Figure 13 shows the measurement layout. The test program and procedures adhered to the specification requirements. Figure 14 illustrates the experimental results of these characteristics in both free space and water debris, revealing the corresponding relationship between the excitation flux and loop current. The x-axis shows the magnetic flux of the telepowering signal received by the balise, while the y-axis depicts the current on its transmitting antenna. This current results from the received magnetic flux processed by internal conversion circuits.

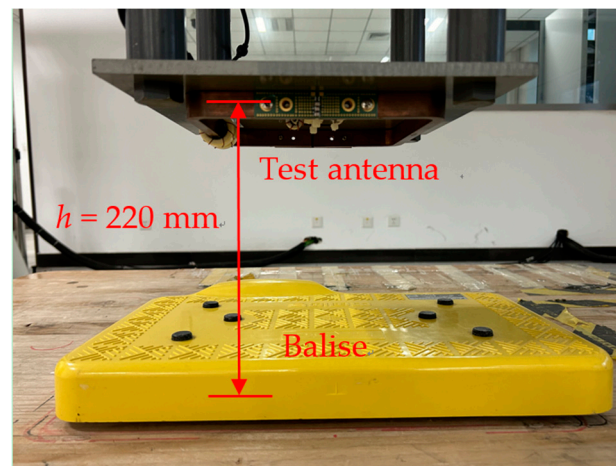


Figure 13. Measurement layout for I/O transfer characteristics.

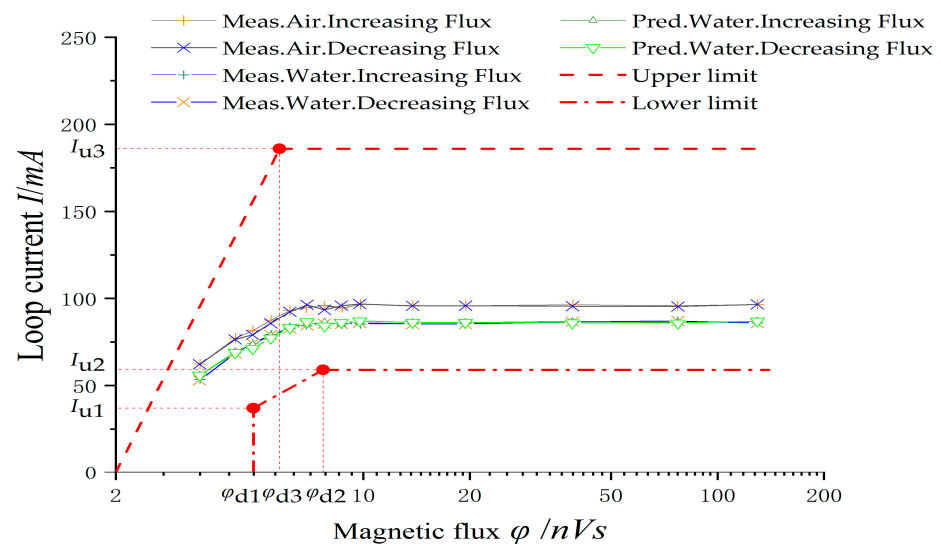


Figure 14. The results of balise I/O transfer characteristics.

The experiments are distributed and included the results of the balise in free space and with underwater debris. Initially, the balise I/O characteristics are measured in free space. The saturated loop current of a balise in free space is approximately 95.2 mA, representing its baseline performance. Subsequently, the characteristics in water debris are predicted using an electrical model, which indicated that the uplink FSK signal attenuation underwater is approximately 0.62 dB greater than in free space. Finally, the balise is measured in water debris, and the actual results were compared with the calculated expectations. When the balise operates in water debris, the current decreases to approximately 86.8 mA due to signal attenuation. The theoretical model predicting the performance calculates a value of 86.9 mA in water debris, which closely aligns with the measured value of 86.8 mA. The minimal difference between the predicted and actual values validates the accuracy of the theoretical model and demonstrates an excellent correlation between the projections and practical observations. The experimental results closely aligned with the calculated predictions.

5. Discussion and Conclusions

This study proposes a quantitative model for analyzing BTS. Leveraging circuit theory, an analytical model of mutual inductance between the OAU and the balise is established, culminating in a formula for calculating the transmission characteristics in water debris.

The analysis examines various position changes of these factors within the main lobe zone. The calculated mutual inductance values and S21 parameters, simulation results, and experimental measurements exhibit generally consistent trends, with the maximum deviation between the calculated and measured S21 parameters not exceeding 0.49 dB, thus demonstrating good agreement. An electrical model is employed to predict the balise I/O characteristics for underwater debris. The uplink FSK signal attenuation in water debris is found to be approximately 0.62 dB greater than in free space, which aligns well with the experimental results. These findings validate the model's accuracy for quantitative analysis of balise transmission performance in water debris. The proposed electrical model facilitates the direct calculation of circuit conditioning parameters and their impact on the transmission characteristics of the BTS, thereby providing valuable insights for product development. The model is validated in a laboratory setting to better control the variables and minimize confounders, allowing for a more accurate study of the specific causal relationships. Utilizing this model, researchers can directly compute circuit conditioning parameters and assess how parameter matching influences the transmission characteristics of BTS. However, the effectiveness of the model in real-world conditions needs to be further verified. Additionally, the prediction model considering transmission loss under various conditions, including the presence of water debris, has significant implications for product development, such as optimizing the OAU transmission power and installation heights of the balise during upgrades. These measures enhance the system reliability and minimize failure risks. The predictions of the model can also aid operators in making informed decisions during adverse conditions, allowing them to take proactive measures to maintain communication integrity.

The rapid growth of high-speed rail networks and BTS has heightened the importance of operational maintenance in product lifecycle management. This focus is essential for ensuring reliability and safety in complex transportation systems. Performance data analysis and electrical modeling have become valuable tools for identifying early failure modes in BTS, potentially preventing more serious issues. These analytical methods offer crucial insights for assessing the current state of BTS and predicting their lifespan, aiding in maintenance planning, performance optimization, and infrastructure longevity. However, while promising in theory, the practical effectiveness of these approaches requires further research and validation. Additional studies are needed to refine these techniques, establish their reliability across various conditions, and determine their long-term impact on system maintenance and performance. As the rail industry evolves, the development of predictive maintenance strategies will likely play an increasingly vital role in ensuring the safety, efficiency, and reliability of high-speed rail systems.

Moreover, the installation of a balise continues to face various challenges. The effectiveness and reliability of the BTS are compromised when the balise is covered with substances such as metallic particles, coal dust, dirt, ice, snow, oils, or other debris. These foreign materials on the surface of the balise degrade its performance and functionality within the BTS. The performance of uplink FSK signals and downlink telepowering signals degrades when installation conditions violate metal-free zone requirements, especially when metal surfaces are present beneath the balise. The electrical model developed in this study needs to be further evaluated. Therefore, the authors propose to develop a system model for installation environments and kinds of debris in subsequent research, facilitating an in-depth investigation into these issues.

Author Contributions: Conceptualization, K.Y. and J.J.; modeling and methodology, K.Y., J.J. and Q.X.; validation, Q.X. and L.Z.; investigation, F.C. and L.Z.; writing—original draft preparation, K.Y.; writing—review and editing, F.C. and L.Z. All authors have read and agreed to the published version of the manuscript.

Funding: This study was supported by the Scientific Research Project (2023YJ288) of China Academy of Railway Sciences Corporation Limited and the Science and Technology Research and Development Program (L2023G011) of China State Railway Group Co., Ltd.

Institutional Review Board Statement: Not applicable.

Informed Consent Statement: Not applicable.

Data Availability Statement: The original contributions presented in the study are included in the article. Further inquiries can be directed to the corresponding author.

Acknowledgments: The authors express their sincere gratitude to all contributors to this study and manuscript. The expertise and dedicated efforts of each contributor were pivotal to the completion of this research. Particular appreciation is extended to Q.X. and L.Z. for their thorough data analysis. Their collaboration ensured the accuracy of the research outcomes. J.J. is acknowledged for her work on simulations and modeling. Their contributions provided a solid theoretical foundation and innovative perspectives for the study. L.Z. is commended for analyzing results and reviewing the modeling and text. This meticulous review deepened the research insights and clarified this paper's presentation. F.C. made significant contributions in data preparation and the provision of essential analysis tools. These efforts were instrumental in facilitating the smooth progress of the research process. In addition, the authors also acknowledge Beijing University of Technology for its invaluable support in conducting the experiments for this study.

Conflicts of Interest: Author Xu Qing is employed by Beijing National Railway Research and Design Institute of Signal and Communication Group Co., Ltd. Author Zhu Linfu works at Standards & Metrology Research Institute, part of the China Academy of Railway Sciences Corporation Limited, which fully owns the China Railway Test & Certification Center. Hence, both institutions were mentioned in his work's submission. Xu Qing and Zhu Linfu confirms there is no commercial conflict of interest related to the paper's publication, reinforcing a commitment to transparency and integrity in academic publishing, without bias or undue commercial influence.

References

1. Muniandi, G. Blockchain-enabled balise data security for train control system. *IET Blockchain* **2021**, *1*, 82–94. [\[CrossRef\]](#)
2. Ali, A.; Smartt, C.; Lester, E.; Williams, O.; Greedy, S. High capacity chipless RFID tags for biomass tracking application. *Int. J. Microw. Wirel. Technol.* **2023**, *15*, 742–752. [\[CrossRef\]](#)
3. UNSIG. SUBSET-036: Form Fit Function Interface Specification for Eurobalise 4.0.0 ed.; UNISIG: Menomonee Falls, WI, USA, 2023.
4. Park, J.; Cho, S. FPGA Implementation for Balise Telegram Decoding and Field Test Validation. *IEEE Intell. Transp. Syst. Mag.* **2022**, *12*, 103–114. [\[CrossRef\]](#)
5. Bian, C.; Yang, S.K.; Xu, Q.Y.; Meng, J.H. Disturbances Prediction of Bit Error Rate for High-Speed Railway Balise Transmission Through Persistent State Mapping. *IEEE Trans. Veh. Technol.* **2022**, *9*, 4841–4849. [\[CrossRef\]](#)
6. Zhang, D.; Wen, Y.H.; Zhang, J.B.; Xiao, J.J.; Song, Y.L.; Geng, Q. Modular System-Level Modeling Method for the Susceptibility Prediction of Balise Information Transmission System. *Appl. Sci.* **2020**, *10*, 7944. [\[CrossRef\]](#)
7. Geng, Q.; Wen, Y.H.; Liu, S.H.; Zhang, D. A VMD Based Improved De-noising of Onboard BTM Receiving Signal. *Chin. J. Electron.* **2020**, *29*, 66–72. [\[CrossRef\]](#)
8. Li, Z.J.; Cai, B.G.; Liu, J.; Lu, D.B. Modelling and performance analysis of Balise under dynamic energy harvesting in high-speed railway. *IET Intell. Transp. Syst.* **2021**, *16*, 1504–1520. [\[CrossRef\]](#)
9. López Díez, P.; Gabilondo, I.; Alarcón, E.; Moll, F. Mechanical energy harvesting taxonomy for industrial environments: Application to the railway industry. *IEEE Trans. Intell. Transp. Syst.* **2020**, *21*, 2696–2706. [\[CrossRef\]](#)
10. Cii, S.; Tomasini, G.; Bacci, M.L.; Tarsitano, D. Solar wireless sensor nodes for condition monitoring of freight trains. *IEEE Trans. Intell. Transp. Syst.* **2021**, *23*, 3995–4007. [\[CrossRef\]](#)
11. Morsi, R.; Jamali, V.; Hagelauer, A.; Ng, D.W.K.; Schober, R. Conditional capacity and transmit signal design for SWIPT systems with multiple nonlinear energy harvesting receivers. *IEEE Trans. Commun.* **2020**, *68*, 582–601. [\[CrossRef\]](#)
12. Adin, I.; Mendizabal, J. A contribution to safe railway operation: Evaluating the effect of electromagnetic disturbances on Balise-to-BTM communication in railway control signaling systems. *IEEE Veh. Technol. Mag.* **2021**, *16*, 104–112.
13. Zhu, L.F.; Li, K.; Wang, J.F.; Xu, B. Study on adaptability of high-speed railway Balise transmission system in complex environment. *J. China Railw. Soc.* **2021**, *43*, 62–69.
14. Tran, M.T.; Thekkan, S.; Polat, H.; Tran, D.D.; El Baghdadi, M.; Hegazy, O. Inductive wireless power transfer systems for low-voltage and high-current electric mobility applications: Review and design example. *Energies* **2023**, *16*, 2953. [\[CrossRef\]](#)
15. Thongpron, J.; Kamnarn, U.; Namin, A.; Sriprom, T.; Chaidee, E.; Janjornmanit, S.; Yachiangkam, S.; Karnjanapiboon, C.; Thounthong, P.; Takorabet, N. Varied-Frequency CC-CV Inductive Wireless Power Transfer with Efficiency-Regulated EV Charging for an Electric Golf Cart. *Energies* **2023**, *16*, 7388. [\[CrossRef\]](#)
16. Hosseini, S.M.; Maghami, M.H.; Amiri, P.; Sawan, M. A 13.56 MHz Low-Power, Single-Stage CMOS Voltage-Boosting Rectifier for Wirelessly Powered Biomedical Implants. *Electronics* **2023**, *12*, 3136. [\[CrossRef\]](#)
17. Bertozzi, M.; Catania, A.; Bandini, G.; Strangio, S.; Iannaccone, G. Load Modulation Feedback in Adaptive Matching Networks for Low-Coupling Wireless Power Transfer Systems. *Electronics* **2023**, *12*, 4619. [\[CrossRef\]](#)

18. Liu, S.; Su, J.; Lai, J.; Zhang, J.; Xu, H. Precise modeling of mutual inductance for planar spiral coils in wireless power transfer and its application. *IEEE Trans. Power Electron.* **2021**, *36*, 9876–9885. [\[CrossRef\]](#)
19. Luo, T.; Zhang, S. Design of underwater wireless power transmission system based on inductive coupling. *J. Mar. Sci. Eng.* **2023**, *11*, 1699. [\[CrossRef\]](#)
20. Allali, N. Enhancing Wireless Charging for Electric Vehicles: Active Load Impedance Matching and Its Impact on Efficiency, Cost and Size. *Energies* **2024**, *13*, 2720. [\[CrossRef\]](#)
21. Di Capua, G.; Femia, N.; Stoyka, K.; Di Mambro, G.; Maffucci, A.; Ventre, S.; Villone, F. Mutual inductance behavioral modeling for wireless power transfer system coils. *IEEE Trans. Ind. Electron.* **2021**, *68*, 2196–2206. [\[CrossRef\]](#)
22. Bertoluzzo, M.; Di Barba, P.; Forzan, M.; Mognaschi, M.E.; Sieni, E. Optimization of compensation network for a wireless power transfer system in dynamic conditions: A circuit analysis approach. *Algorithms* **2022**, *15*, 261. [\[CrossRef\]](#)
23. Jeon, S.J.; Lee, S.H.; Seo, D.W. Unilateral route method to estimate practical mutual inductance for multi-coil WPT system. *Electronics* **2020**, *9*, 377. [\[CrossRef\]](#)
24. UNSIG. SUBSET-085: Test Specification for Eurobalise FFFIS 4.0.0 ed.; UNISIG: Menomonee Falls, WI, USA, 2023.
25. Zhao, L.; Jiang, Y. Modeling and optimization research for dynamic transmission process of balise tele-powering signal in high-speed railways. *Prog. Electromagn. Res.* **2013**, *140*, 563–588. [\[CrossRef\]](#)
26. Kim, J.; Kim, D.H.; Kim, J.; Park, Y.J. Wireless power transfer between two self-resonant coils over medium distance supporting optimal impedance matching using ferrite core transformers. *Energies* **2021**, *14*, 8540. [\[CrossRef\]](#)
27. Zhang, K.; Ma, Y.; Yan, Z.; Di, Z.; Song, B.; Hu, A.P. Eddy current loss and detuning effect of seawater on wireless power transfer. *IEEE J. Emerg. Sel. Top. Power Electron.* **2020**, *8*, 909–917. [\[CrossRef\]](#)
28. Oarkan, T.; Zhang, P.; Shih, C. Analysis, design, and maximum power-efficiency tracking for undersea wireless power transfer. *IEEE J. Emerg. Sel. Top. Power Electron.* **2018**, *6*, 843–854. [\[CrossRef\]](#)
29. Yan, Z.; Zhang, Y.; Kan, T.; Lu, F.; Zhang, K.; Song, B.; Mi, C.C. Frequency optimization of a loosely coupled underwater wireless power transfer system considering eddy current loss. *IEEE Trans. Ind. Electron.* **2019**, *66*, 3468–3476. [\[CrossRef\]](#)
30. Luo, Z.; Wei, X. Analysis of square and circular planar spiral coils in wireless power transfer system for electric vehicles. *IEEE Trans. Ind. Electron.* **2017**, *65*, 331–341. [\[CrossRef\]](#)
31. Acero, J.; Carretero, C.; Lope, I.; Alonso, R.; Lucia, Ó.; Burdio, J.M. Analysis of the mutual inductance of planar-lumped inductive power transfer systems. *IEEE Trans. Ind. Electron.* **2013**, *60*, 410–420. [\[CrossRef\]](#)
32. Kim, J.; Kim, K.; Kim, H.; Kim, D.; Park, J.; Ahn, S. An efficient modeling for underwater wireless power transfer using Z-parameters. *IEEE Trans. Electromagn. Compat.* **2019**, *61*, 2006–2014. [\[CrossRef\]](#)
33. Cheng, Z.; Lei, Y.; Song, K.; Zhu, C. Design and loss analysis of loosely coupled transformer for an underwater high-power inductive power transfer system. *IEEE Trans. Magn.* **2015**, *51*, 1–10.
34. Jenkins, A.; Bana, V.; Anderson, G. Impedance of a coil in seawater. In Proceedings of the 2014 IEEE Antennas and Propagation Society International Symposium (APSURSI), Memphis, TN, USA, 6–11 July 2014; pp. 625–626.
35. Couraud, B.; Deleruyelle, T.; Kussener, E.; Vauché, R. Real-time impedance characterization method for RFID-type backscatter communication devices. *IEEE Trans. Instrum. Meas.* **2018**, *67*, 288–295. [\[CrossRef\]](#)

Disclaimer/Publisher’s Note: The statements, opinions and data contained in all publications are solely those of the individual author(s) and contributor(s) and not of MDPI and/or the editor(s). MDPI and/or the editor(s) disclaim responsibility for any injury to people or property resulting from any ideas, methods, instructions or products referred to in the content.